

pubs.acs.org/ac Article

Effective Electrochemical Modulation of SERS Intensity Assisted by Core—Shell Nanoparticles

Jing Guo, Xingxu Yan, Mingjie Xu, Govinda Ghimire, Xiaoqing Pan, and Jin He*



Cite This: Anal. Chem. 2021, 93, 4441-4448



Read Online

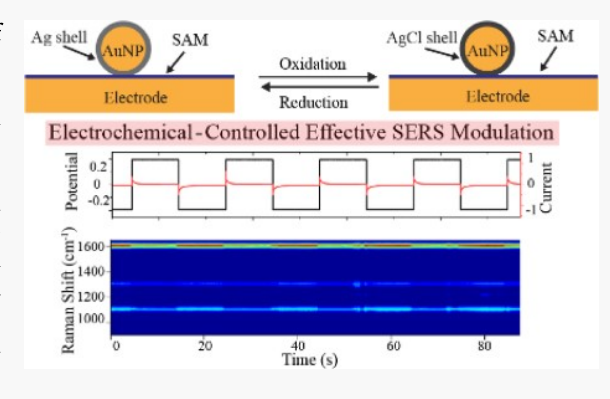
ACCESS

III Metrics & More

Article Recommendations

Supporting Information

ABSTRACT: An effective and reversible tuning of the intensity of surface-enhanced Raman scattering (SERS) of nonelectroactive molecules at nonresonance conditions by electrochemical means has been developed on plasmonic molecular nanojunctions formed between Au@Ag core—shell nanoparticles (NPs) and a gold nanoelectrode (AuNE) modified with a self-assembled monolayer. The Au@Ag nanoparticle on nanoelectrode (NPoNE) structures are formed in situ by the electrochemical deposition of Ag on AuNPs adsorbed on the AuNE and can be monitored by both the electrochemical current and SERS signals. Instead of introducing molecular changes by the applied electrode potential, the highly effective SERS intensity tuning was achieved by the chemical composition transformation of the ultrathin Ag shell from metallic Ag to insulating AgCl. The electrode potential-induced electromagnetic enhancement (EME) tuning in the Au@Ag



NPoNE structure has been confirmed by finite-difference time-domain simulations. Moreover, the specific Raman band associated with Ag—molecule interaction can also be tuned by the electrode potential. Therefore, we demonstrated that the electrode potential could effectively and reversibly modulate both EME and chemical enhancement in Au@Ag NPoNE structures.

■ INTRODUCTION

Surface-enhanced Raman scattering (SERS) has become a powerful molecular spectroscopy tool to probe molecules in plasmonic nanostructures, and a wide range of applications in materials, electronics, energy, environment, agriculture, and biomedical fields have been demonstrated. Controllable modulation of SERS intensity of molecules can further empower the SERS technique for fundamental studies and various applications. Compared with other means, electrochemical (EC) modulation is effective and convenient to use. The integration of electrochemistry and SERS has been proven to be highly useful for surface and interfacial studies^{2–8} biochemical and biosensing applications. 9-13 The SERS enhancement mechanisms are well-known: electromagnetic enhancement (EME) and chemical enhancement (CME). In previous studies, the tuning of SERS intensity by the EC potential is mainly based on the CE change because of the potential-controlled molecule changes, including the redox states of the molecule, the metal-molecule interactions, and the molecule geometry and orientations. Most of the reported SERS changes modulated by the EC potentials are from the chemical transformations of electroactive molecules. 14-16 For nonelectroactive molecules, the SERS intensity modulation has been observed due to the potential-dependent molecular geometry⁵ or orientation changes.² It is also important to consider that the EC potential induced changes in the optical properties of plasmonic substrates, 17-19 such as localized

surface plasmon resonance (LSPR) and substrate—molecule charge transfer. The properties of the molecule, plasmonic substrate, and substrate—molecule interaction all play important roles in the observed SERS spectra of plasmonic molecular junctions and can be utilized to achieve highly effective and reversible SERS intensity modulation by the EC potential.

Herein, we demonstrate that the SERS intensity of plasmonic molecular junctions with nonelectroactive molecules can also be effectively modulated at nonresonance conditions by the electrode potential after introducing an ultrathin silver layer at the molecule—metal interface in the plasmonic nanostructures. It has been demonstrated that reversible and active tuning of plasmonic field enhancement by the electrode potential can be achieved on plasmonic AuNPs coated with a thin Ag layer. ^{21–23} The dramatic optical property changes are attributed to the changes of LSPR of NPs during the reversible redox process of the Ag layer regulated by the electrode potential. The excitation of LSPR in plasmonic substrates is the

Received: October 18, 2020 Accepted: February 17, 2021 Published: March 2, 2021





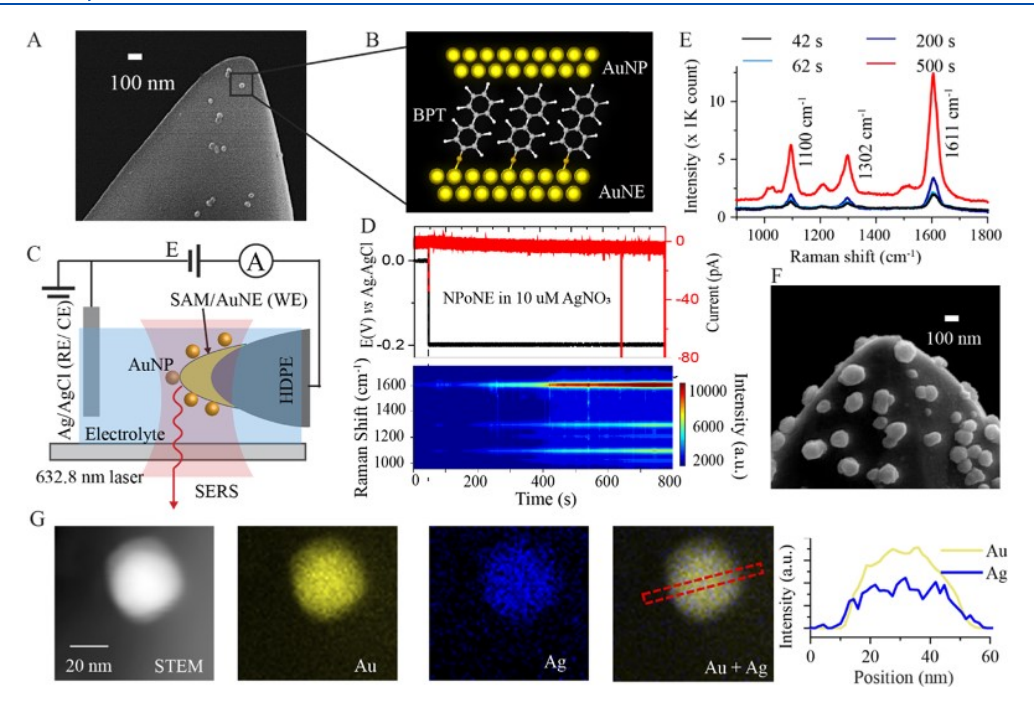


Figure 1. Fabrication of Au@Ag NPoNE structures. (A) SEM image of BPT-modified AuNE apex with adsorbed AuNPs. To improve the SEM image quality, the AuNE was not insulated. (B) Plasmonic BPT molecular junctions in the Au NPoNE structure. (C) Scheme of the experimental setup for the EC-SERS measurements. The AuNE is partially insulated by high-density polyethylene. The electrode potential E was applied to the WE AuNE, and the Ag/AgCl wire electrode was the quasi-reference electrode (RE) and counter electrode (CE). (D) Top panel: chronoamperogram of Ag deposition. The applied electrode potential (solid black line) and acquired electrochemical current (solid red line) are plotted. Bottom panel: the corresponding SERS intensity heatmap. The exposure time for SERS is 0.1 s/frame. (E) Selected SERS spectra from the heatmap before Ag deposition at t = 42 s and after Ag deposition at t = 62, 200, and 500 s. (F) SEM image of a AuNE apex with Au@Ag NPs after 30 min of Ag deposition. (G) Scanning transmission electron microscopy (STEM) image and element analysis by energy-dispersive X-ray spectroscopy (EDS) of a Au@Ag core—shell NP formed after 30 s Ag deposition. Distribution of Au and Ag component in the Au@Ag core—shell NP obtained by the rectangle-scan analysis which is indicated as a red dashed box.

critical factor for achieving significant EME in SERS.²⁴⁻²⁶ Therefore, we expect that the SERS intensity can be tuned in the same fashion by forming plasmonic molecular junctions using Au@Ag core-shell NPs. The experiment was performed by using an NP on the nanoelectrode (NPoNE) geometry (see Figure 1). We have demonstrated that the NPoNE geometry can provide single-molecule level sensitivity with a 10 s of ms time resolution at a relatively low laser power. 27-29 Because of the ultrasmall exposed tip area of the gold nanoelectrode (AuNE), the NPoNE geometry is advantageous in EC-SERS measurements for higher sensitivity and better correlation between the EC current and SERS signals. After AuNPs were adsorbed on the molecule-modified AuNE surface, an ultrathin shell of silver was electrochemically deposited in situ on the surface of adsorbed AuNPs. The thickness of the silver shell can be controlled by the silver deposition time and estimated from the electrochemical current. With the presence of chloride ions in solution, the shell can be converted from Ag to AgCl by the applied positive electrode potential, leading to a significant reduction of EME in the nanocavity. With the optimization of shell thickness, the reversible SERS intensity change up to two times could be achieved in a small electrode potential window. The intensity modulation by the electrode potential is achieved by EME, while the molecules remain unchanged. However, for molecules having a stronger interaction with Ag atoms, bigger SERS intensity tuning by the electrode potential can be achieved on specific vibrational bands with the contributions from both EME and CME modulations.

EXPERIMENTAL SECTION

The details of electrochemical etching, insulation, and characterization of AuNEs have been reported previously. ^{27,30} The tip of the cleaned AuNE was soaked in 5 mM molecule

Fabrication and Chemical Modification of the AuNE.

The tip of the cleaned AuNE was soaked in 5 mM molecule [BPT or 4-MBA (4-mercaptobenzoic acid)] ethanol solution various times from 7 h to overnight. The chemically modified AuNE was then rinsed thoroughly with ethanol and dried with

argon gas.

Formation of Au@Ag NPoNE Structures. The AuNE covered with a SAM was immersed in a 75 pM 40 nm AuNP aqueous solution for 20 min and then rinsed to remove weakly attached AuNPs. Because the current is small in the EC measurements, a two-electrode system was used. The SAM-modified AuNE with adsorbed AuNPs was used as the working electrode (WE), and the Ag/AgCl wire was used as both the quasi RE and CE. For Ag deposition, the chronoamperometry setup was used at a constant electrode potential of -0.2 V in $10 \ \mu\text{M}$ AgNO₃. The deposition potential is chosen based on the reduction potential of Ag⁺ ions on the AuNE (see Figure S1); the details of simultaneous EC and SERS measurements can be found in Supporting Information S2. The time resolution of SERS spectra is normally 0.1 s/frame, if not mentioned otherwise.

TEM Methods. High-angle annular dark-field (HAADF) STEM imaging and EDS mapping were carried out using JEOL-JEM300CF double aberration-corrected TEM, operating at 300 kV. The Au tip was mounted on a Hummingbird

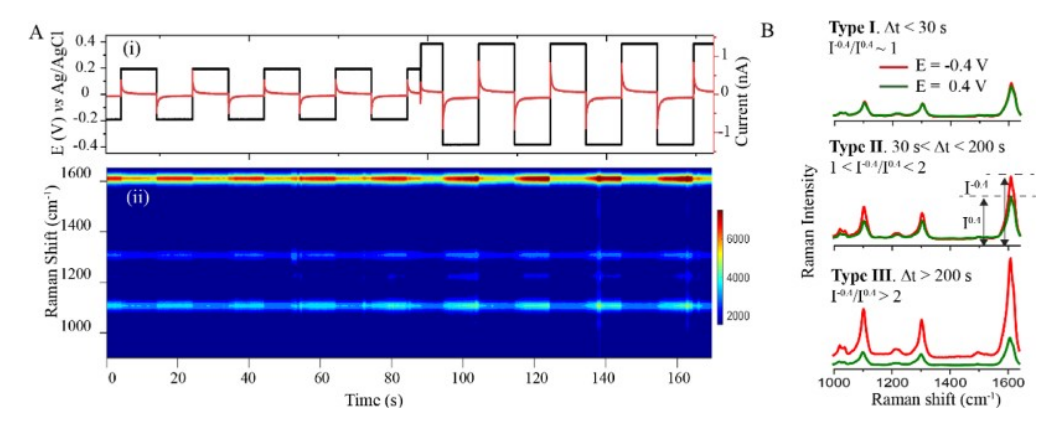


Figure 2. SERS intensity tuning at different Ag deposition times Δt . (A) (i) Top panel: the double potential step chronoamperogram shows the applied potential waveform (black trace) on the Au@Ag NPoNE and recorded EC current (red trace) in 1× PBS. The period of the square potential waveform is 20 s. The exposure time for SERS is 0.1 s/frame. (ii) Bottom panel: the corresponding SERS intensity heatmap of BPT. This structure is formed with a Ag deposition time $\Delta t = 180$ s. (B) Typical SERS spectra of BPT from three types of Au@Ag NPoNE structures at E = -0.4 V (red color) and +0.4 V (olive color).

Scientific single-tilt tomography holder with a home-made sample clamp tip. EDS was conducted using JEOL dual EDS detectors.

Simulation Methods. Modeling and simulations were performed using the finite difference time domain (FDTD) method (Lumerical's Multiphysics software). The modeling structures are discussed in the Results and Discussion section. The refractive index of the water medium is 1.33. The dielectric functions of Au and Ag used in the simulation are from experimental data of the Johnson and Christy handbook.³¹ The refractive index of AgCl is 2.02.^{32,33} The small difference in the dielectric function of Ag between the ultrathin film and bulk is ignored.

■ RESULTS AND DISCUSSION

Formation of the Au@Ag NPoNE Structure. The exposed apex area of the partially insulated AuNE is in the range of 30–80 μ m² (see S3). A monolayer of biphenyl-4-thiol (BPT) was self-assembled on the AuNE apex. Figure 1A shows the typical scanning electron microscopy (SEM) image of a BPT-modified AuNE tip (not insulated) after immersion in the solution with 40 nm AuNPs. The average number density of the adsorbed AuNPs on the exposed AuNE apex is about 11 μm^{-2} (see Supporting Information S4). A typical laser spot focused on the AuNE apex can cover up to ~50 adsorbed AuNPs. Plasmonic molecular junctions are formed in these Au NPoNE structures, as shown in Figure 1B. Using the setup illustrated in Figure 1C, Ag was selectively deposited on the surface of the adsorbed AuNPs on the AuNE apex. The deposition was carried out by the chronoamperometry method at a reduction potential of -0.2 V with 10 μ M AgNO₃ in the electrolyte.²² The amount of deposited Ag was controlled by the deposition time, which varied from 20 to 600 s. Figure 1D shows the time-resolved changes of simultaneously acquired reduction current (top panel, red color trace) and SERS signals in the intensity heatmap (bottom panel) during the Ag deposition. While the reduction current magnitude increases (more negative) slightly, the SERS intensity increases significantly with the deposition time. The rapid increase of SERS intensity is also demonstrated in Figure 1E, showing four SERS spectra at different times sampled from the SERS trajectory in Figure 1D. All spectra show three major peaks of BPT (see the Supporting Information S5 section, assignment

of BPT Raman peaks), confirming the formation of NPoNE structures containing BPT molecular junctions.

Figure 1F shows the SEM image of a AuNE apex after 30 min of Ag deposition. The size of Au@Ag NPs is much bigger than the initial 40 nm size of AuNPs. It should be noted that the 30 min deposition time is much longer than the actual time used for SERS measurements, which is only used here to visualize the Ag deposition by SEM. It is clear that the silver deposition mainly happens on the adsorbed AuNPs. The STEM image in Figure 1G shows a Au@Ag NP formed on the AuNE apex after 30 s of Ag deposition. The NP size is still about 40 nm. The element analysis by EDS reveals the welldistributed Ag on the Au NP, confirming the formation of Au@Au and the ultrathin Ag layer. It has been well-studied that metal NP-mediated electron transfer across an insulating thin film, such as SAM, is highly effective.³⁴ Therefore, the adsorbed AuNPs can serve as the nucleation sites for Ag deposition. The BPT SAM helps to prevent random silver deposition and facilitates the in situ fabrication of Au@Ag core-shell NPs on the AuNE apex, leading to the formation of Au@Ag NPoNE structures and the enhancement of SERS intensity. The bigger number density of NPs on the AuNE apex after 30 min of Ag deposition also suggests that pure Ag NPs can indeed form on the SAM, which is likely through the SAM defects. However, the possibility should be very small within 5 min of Ag deposition due to the preferred deposition on the adsorbed Au NPs. In addition, even though some pure Ag NPs are formed, their size should be quite small within 5 min of Ag deposition. Their SERS contribution should be much smaller than the Au@Ag core-shell NPs at an excitation laser wavelength of 633 nm³⁵ (see more discussion in Supporting Information section S6). In this work, we have ignored the possible formation of pure Ag NPs within 5 min of Ag deposition.

Reversibility of SERS Intensity Modulation by the Potential. To evaluate the efficiency and reversibility of the potential modulation of SERS intensity, we performed double potential step chronoamperometry on the fabricated Au@Ag NPoNE structures in the $1 \times$ PBS electrolyte. The silver atom was oxidized to become a silver ion (Ag^+) at the positive potential step, and the Ag^+ ion was reduced back to a Ag atom at the negative potential step. In a representative current—time trace (i) of Figure 2A, a current spike appears at the beginning

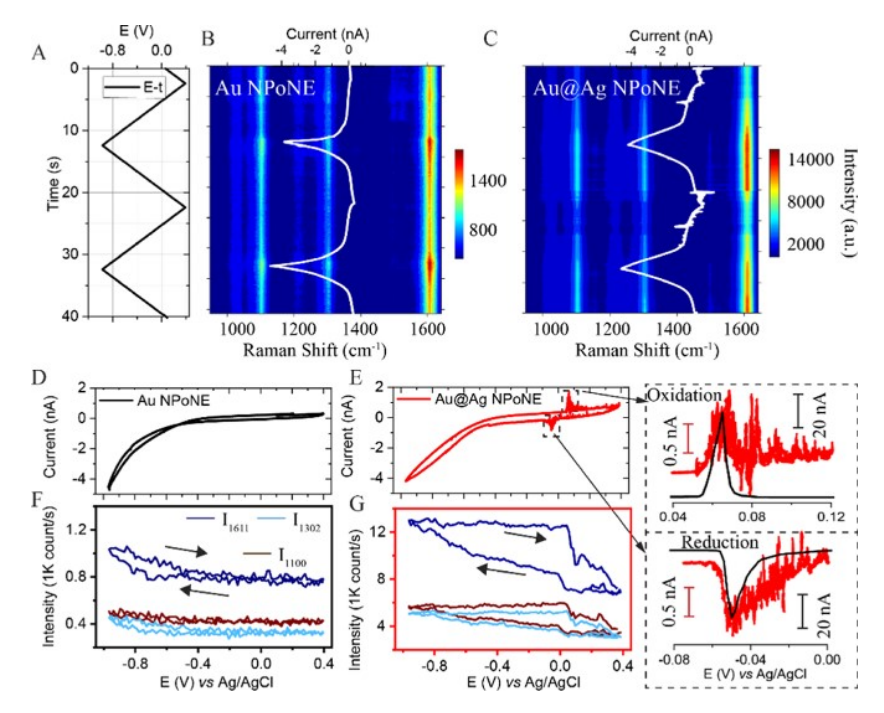


Figure 3. Comparison of CV and SERS measurements of Au and Au@Ag NPoNE structures. (A) The triangle waveform was applied to the AuNE in the 1× PBS electrolyte. Sweep rate: 0.14 V/s. (B–C) SERS intensity heatmap of BPT in the nanocavities of the Au NPoNE (B) and Au@Ag NPoNE (C) structures. SERS spectra were recorded at 10 frame/s. The EC current (solid white line) is superimposed on the heatmap. (D–G) EC current (D,E) and SERS intensity (F,G) of three main peaks of BPT as a function of E for the Au NPoNE (D,F) and Au@Ag NPoNE (E,G) structures. Arrows indicate the sweeping direction of E. Right panel: the zoom-in view of oxidation and reduction peaks of silver on the NPoNE. The oxidation and reduction peaks of a silver microelectrode (black line) are added as the reference.

of each square wave, which is due to the charging current. Following the decay of charging current, a stable Faraday current plateau due to the Ag redox reaction appears. The magnitude of the Faraday current is bigger when the step potential magnitude is increased from 0.2 to 0.4 V, indicating that more Ag atoms are involved in the redox process at the higher potential.

The bottom panel (ii) of Figure 2A shows the corresponding SERS trajectory. The SERS intensity of the BPT molecule is higher at -0.4 V than that at -0.2 V, which is consistent with the higher EC current at -0.4 V. The SERS intensity is clearly modulated by the potential as low as ± 0.2 V, demonstrating that the potential modulation is highly effective. The potential modulation is also highly reversible at both potential magnitudes. We also notice that the SERS intensity change is slower when the electrode potential decreased from +0.4 to -0.4 V but much faster when the electrode potential increased from -0.4 to +0.4 V (see the zoom-in view with more details in Figure S10B). This is attributed to the slower reduction kinetics of Ag⁺ ions (see the next section), which has been observed for the reduction of Ag⁺ from the solution and on the surface of Au@Ag core—shell NPs. $^{2.1,36}$

The reversibility of the SERS intensity modulation also depends on the thickness of the Ag shell. Based on the magnitude and reversibility of the SERS intensity ratio at ± 0.4 V ($I^{-0.4}/I^{0.4}$), the performance of the prepared Au@Ag NPoNE structures can be divided into three types, which is clearly associated with the silver deposition time Δt (thus the thickness of the Ag shell). Here, $I^{-0.4}$ is defined as the SERS intensity of the peak at 1611 cm⁻¹ after subtracting the baseline when E=-0.4 V. The baseline is defined as the average SERS intensity in the range from 1340 to 1440 cm⁻¹,

where no Raman peaks are present. Figure 2B shows the typical SERS spectra pair of all three types. Type I structures are normally obtained when $\Delta t < 30$ s. For this type, $I^{-0.4}/I^{0.4}$ is close to 1. The short deposition time leads to a thin and incomplete shell, resulting in a negligible intensity change. Type II structures are obtained when Δt is between 30 and 200 s. The intensity modulation ratio is between 1 and 2, and the modulation is highly reversible. The example in Figure 2A belongs to this type. Type III structures are obtained when Δt > 200 s. For this type, the intensity modulation ratio is bigger than 2, although the reversibility is compromised (see an example in Supporting Information section S7 and Figures S5 and S6). For the thick Ag/AgCl layer, some Ag⁺ ions are likely dissolved in the solution, leading to the gradual reduction of SERS intensity in the repeated potential modulation cycles. This type of structure can be useful in applications when large intensity modulation is desired and reversibility is not important.

Mechanism of Silver Shell-Assisted Large Modulation of SERS Intensity by the Electrode Potential. We further investigated the mechanism of silver shell-assisted potential modulation of SERS intensity based on reversible type II Au@ Ag NPoNE structures. To understand the redox reaction of the shell, cyclic voltammetry (CV) and SERS measurements were conducted simultaneously. As shown in Figure 3A, the electrode potential was swept between -1 and 0.4 V in the $1 \times PBS$ solution. The acquired EC current—time (i-t) traces (white color) are superposed on the SERS intensity heatmaps in Figure 3B,C. Stochastic current spikes appear in the i-t trace of Figure 3C. The corresponding CVs of AuNPs without (black curve) and with (red curve) Ag shells are shown in Figure 3D,E, respectively. In both CVs, the obvious current

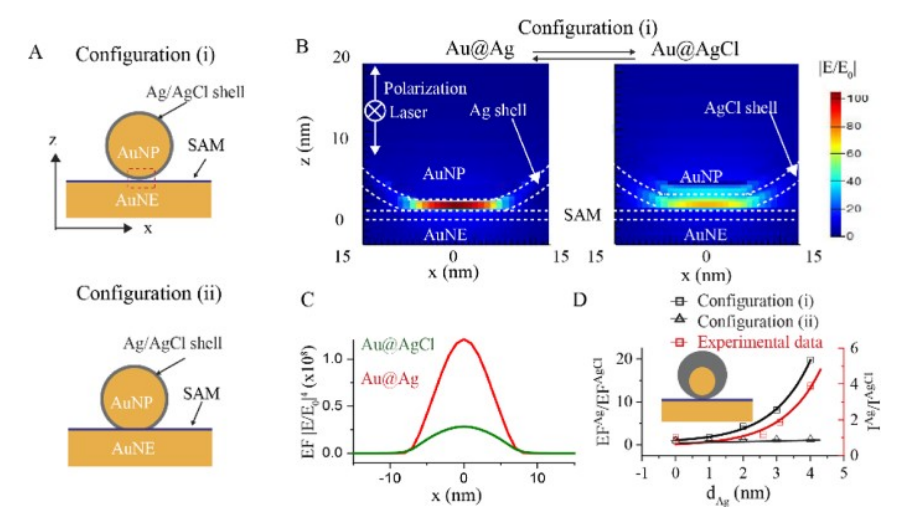


Figure 4. FDTD simulations of EC modulation of the EME mechanism in the cavity of the Au@Ag NPoNE structure. (A) Two possible configurations of Au@Ag NPoNE structures. (B) $|E/E_0|$ distribution in the nanogap of configuration (i) with Ag (left) and AgCl (right) shell of 2 nm thickness. The incident direction and polarization of 632.8 nm light are shown. (C) Electric field enhancement (EF) distribution at the center of SAM (z = 0.65 nm) along the x-axis in the nanogap of the Ag shell (red color) and AgCl shell (olive color). (D) Left y-axis: FDTD simulation results of EF^{Ag}/EF^{AgCl} at x = 0 and z = 0.65 nm as a function of d_{Ag} for configuration (i) (black open squares) and configuration (ii) (black open triangles). The black solid line is the fit by the exponential equation: $0.55 \times \exp\left(d_{Ag}/1.12\right) + 0.54$ ($R^2 = 0.99$). Right y-axis: Red open squares are experimental data at 1611 cm⁻¹ of BPT, which are fitted by the exponential equation: $0.55 \times \exp\left[(d_{Ag}-2)/1.12\right] + 0.54$ (red line, $R^2 = 0.99$).

drop beyond -0.4 V is attributed to the hydrogen evolution reaction (HER). Figure 3F,G shows the corresponding intensity changes of three main SERS peaks of BPT as a function of E. As shown in Figure 3F, the modest SERS intensity increases of all three peaks are only observed at the negative potential beyond -0.4 V. The correlation coefficient of the current magnitude and SERS intensity is 0.86, indicating a strong correlation between HER and SERS intensity enhancement, which has been reported in previous research. ^{17,18} The pH-dependent experiments, as shown in the Supporting Information S8 section, further confirm the role of HER in SERS intensity enhancement.

The CV in Figure 3E of Au@Ag NPoNE structures shows new oxidation peaks at $E_1 = 0.07 \text{ V}$ and reduction peaks at $E_2 =$ -0.05 V. This pair of redox peaks should be from the redox reaction of Ag/AgCl on the surface of adsorbed AuNPs.²⁰ The oxidation potential to form Ag₂O is much higher at about 0.4 V. 37,38 In addition, in the control experiment without chloride ions in the solution, no oxidation peaks were observed in the same potential range (see Supporting Information S9). The small oxidation and reduction peaks in the CV are expanded on the right side of Figure 3E. It is clear that the redox peaks are composed of a series of stochastic spikes (also see Figure 3C). For comparison, the redox peaks from a silver microelectrode have the same peak positions but are rather smooth. The stochastic nature of Ag/AgCl redox peaks suggests that only a limited number of silver atoms are involved in the redox process. Figure 3G shows the significant SERS intensity jump near the Ag/AgCl redox potential of all three bands of BPT. The HER-induced SERS intensity change beyond -0.4 V is much smaller. Therefore, the effective SERS modulation is attributed to the reversible redox process Ag + Cl⁻ ↔ AgCl + e⁻ happened at the Ag shell of the Au@Ag NPoNE. To avoid HER, a potential range between -0.4 and 0.4 V was used in most of our experiments. In this potential range, the SERS intensity modulation is mainly induced by the potential-controlled chlorination/dechlorination of the Ag/

AgCl shell. As we mentioned earlier, the level of modulation can be defined by the intensity ratio of $I^{-0.4}/I^{0.4}$ (or I^{Ag}/I^{AgCl}). Here, $I^{-0.4}/I^{0.4}$ at 1611 cm⁻¹ is only 1.09 for the Au NPoNE but increases to 1.78 for the Au@Ag NPoNE.

Simulations of EME in Au@Ag and Au@AgCl NPoNE Structures. To better understand the geometry of the nanocavity and the potential modulation mechanism, we have simulated the EME change in the NPoNE nanocavity induced by the Ag/AgCl transformation using the FDTD method. Figure 4A shows the schemes of two configurations based on the possible structure of the shell. More configurations were discussed in Supporting Information S8. The 40 nm AuNP, which is covered with a uniform Ag shell, sits on a AuNE surface modified with a SAM. Considering the BPT SAM, we used a thickness of 1.3 nm with a refractive index n = 1.45 based on the previous report.³⁹ For configuration (i), Ag covers the whole AuNP surface, leading to a full shell and a Au/Ag-molecule-Au junction configuration in the cavity. For configuration (ii), the Ag deposition only happens on the exposed surface of the adsorbed AuNP but does not penetrate into the nanogap, leaving an incomplete shell and no Ag inside the nanogap. Figure 4B (left) shows the normalized electric field amplitude ($|E/E_0|$) distribution across the nanogap of the configuration (i) with a Ag shell of 2 nm thickness. $|E_0|$ is the electric field amplitude of the incident laser. Because the AuNPs typically have different facets, 40 we used a facet diameter of 13 nm for the 40 nm AuNPs to form the nanogap. The greatest field strength appears in the nanogap across the SAM, which is the so-called "hotspot". Figure 4B (right) shows the $|E/E_0|$ distribution in the same structure when the Ag shell is changed to the AgCl shell. In the experiment, when Ag is transformed to AgCl, the shell thickness should be slightly bigger due to the intercalation of chloride ions. For simplicity, we still assume that the AgCl shell thickness remains as 2 nm here. Inside the nanogap, the $|E/E_0|$ is greatly reduced in the SAM and its distribution is also extended into the AgCl shell.

Figure 4C compares the enhancement factor (EF) in the center of the SAM inside the nanogap of (B,C) as a function of x position for both Ag and AgCl shells. The EF is the fourth power of $|E/E_0|$. The maximum EF was denoted as EF^{Ag} and EF^{AgCl} when the shell is Ag and AgCl, respectively. The EF^{Ag} is several times higher than EFAgCl. As shown in Figure 4D, we also calculated EF^{Ag}/EF^{AgCl} as a function of shell thickness d_{Ag} for configuration (i) (black open squares) and (ii) (black open triangles). The EF^{Ag}/EF^{AgCI} of configuration (i) shows an exponential increase with d_{Ag} . The EF^{Ag}/EF^{AgCl} of configuration (ii) remains about 1 at different d_{Agr} showing almost no intensity modulation by the shell transformation from Ag to AgCl (also see Supporting Information S10). The experimental data (red solid squares) are also plotted for comparison. The d_{Ag} of experimental data is estimated based on the total charge transferred during the AgCl/Ag redox process under the assumption that the Ag shell is uniform on the surface of AuNPs (see detailed calculation in Supporting Information S10). The experimental data of $I^{Ag}/I^{\hat{AgCl}}$ are between the simulated EF_{Ag}/EF_{AgCl} data of configurations (i) and (ii), suggesting that the shell thickness in the nanogap is thinner than the estimation of configuration (i). It is reasonable to expect that less Ag is deposited inside the nanogap, considering the hindered diffusion of Ag⁺ ions into the nanogap. Thus, a more realistic configuration is proposed, as shown in the inset of Figure 4D. We found that the experimental data can be fitted by the same exponential decay equation as the simulated data of configuration (i) after substituting d_{Ag} with $(d_{Ag} - 2)$, supporting the proposed nonuniform shell thickness configuration.

EC Modulation of Chemical Enhancement. Without introducing molecular transformation and geometry and orientation changes, the SERS intensity may still be modulated by the electrode potential through the CME mechanism due to the change of the molecule-shell interaction. Molecule 4-MBA (see Figure 5A) has been used for the investigation of various CME mechanisms in SERS. 41-48 The scheme in Figure 5A illustrates the interaction between the deprotonated carboxyl group of 4-MBA and Ag but not AgCl. As shown in Figure 5B, a square-wave potential was applied to the 4-MBA-modified AuNE to modulate the Ag/AgCl transformation of the shell. The SERS intensities of all 4-MBA vibration peaks are high at E = -0.4 V and low at E = 0.4 V. The intensity modulation by the electrode potential is fully reversible over continued cycles, which is consistent with the case of the BPT molecule in type II structures. Same as the BPT molecule, a slower SERS intensity change during the dechlorination of the AgCl layer (reduction of Ag+ ions) is also observed (see Figure S11C). Because of the Ag shell-4-MBA interaction, the CME mechanism also contributes to the observed intensity increase at the negative potential. To decouple the CME from the EME, the intensity of the spectra can be normalized to I_{1077} of ν (C–S), which is mainly affected by the EME but less affected by the CME induced by the Ag-COO⁻ interaction. Figure 5C shows two normalized SERS spectra taken from two time spots in the SERS trajectory of Figure 5B, indicated by the red and green dashed lines. The biggest spectral change happens near 1392 cm⁻¹, which is from the stretching mode of COO⁻. This mode is greatly enhanced by the interaction with the Ag atom at -0.4 V. In addition, smaller relative intensity increases of the aromatic ring $\nu(C-C)$ vibration mode at 1588 cm⁻¹ were observed in the normalized spectra at -0.4 V, which is also affected by the CME.

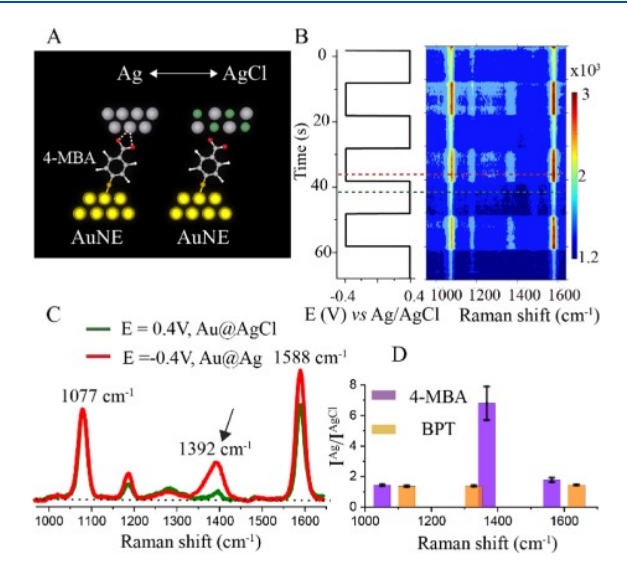


Figure 5. EC modulation of CME. (A) Illustration of the moleculemetal interaction between the deprotonated carboxyl group of 4-MBA and Ag or AgCl. (B) SERS intensity heatmap of 4-MBA in the nanocavity of the Au@Ag NPoNE as a function of electrode potential in square waveform (IEI = 0.4 V, $T=20~\rm s$). The exposure time for SERS is 0.2 s/frame. The Ag deposition time is 150 s. (C) Selected SERS spectra at $E=-0.4~\rm V$ ($t=75~\rm s$) and $E=0.4~\rm V$ ($t=82~\rm s$) from the heatmap in (B). The spectra are normalized at 1077 cm⁻¹. The black dashed line is the baseline of Raman spectra. (D) Average intensity ratio $I^{\rm Ag}/I^{\rm AgCl}$ of three main bands for both BPT and 4-MBA molecules. The error bar is the calculated standard deviation of three experiments with three different AuNEs.

Figure 5D summarizes the average intensity ratio $I^{\rm Ag}/I^{\rm AgCl}$ of three major SERS peaks for both 4-MBA and BPT molecules in three type II structures. The ratio is ~ 1.6 for all three bands of BPT and two bands of 4-MBA. The modulation of these bands is mainly attributed to the EME mechanism, as discussed in the FDTD simulation. However, the ratio is ~ 6.8 for the band at 1392 cm⁻¹ of 4-MBA. The selective enhancement of additional 4.5 times for this specific band is mainly attributed to the CME induced by the specific carboxylate—Ag interaction.

CONCLUSIONS

In summary, this study shows that effective and reversible electrochemical tuning of SERS intensity of nonelectroactive molecules can be achieved with the assistance of the chemical transformation at the shell of shell-core plasmonic NPs. The Au@Ag NP can be formed in situ on the SAM-covered AuNE surface, and the formation of the Ag shell can be interrogated in real time through monitoring both the EC current and SERS changes. When the electrode potential was swept on the formed Au@Ag NPoNE structures, the simultaneously acquired EC current and SERS revealed the strong correlation between the redox reaction of the silver shell and the SERS intensity modulation. The degree and reversibility of SERS tuning were controlled by the Ag deposition time on AuNPs, as well as the Ag shell thickness. 3D-FDTD simulation confirmed that the EME modulation is mainly due to the large refractive index change of the shell when the metallic Ag is converted to insulating AgCl. In addition to the modulation of EME, the CME can also be modulated during the chlorination of the Ag shell. The specific interaction between the molecule

end group and shell, which is affecting the polarization of molecule, can be switched on and off during the chemical conversion of the shell between Ag and AgCl. The combination of EME and CME modulations can further boost the tuning effect. The electrode potential tunable SERS based on the Au@Ag NPoNE geometry can help to better understand the EME and CME mechanisms in plasmonic molecular junctions. The electrode potential also provides a facile and fast means to tune the SERS intensity of a wide range of molecules in the plasmonic molecular nanostructures and devices, and the reported method can trigger new EC-SERS applications in electroanalysis, heterogeneous catalysis, plasmonics, molecular electronics, and biosensing.

ASSOCIATED CONTENT

Supporting Information

The Supporting Information is available free of charge at https://pubs.acs.org/doi/10.1021/acs.analchem.0c04398.

Methods, NP number density estimation, assignment of BPT Raman peaks, FDTD simulation of possible configurations, and Ag shell thickness estimation (PDF)

AUTHOR INFORMATION

Corresponding Author

Jin He — Department of Physics and Biomolecular Science Institute, Florida International University, Miami, Florida 33199, United States; ⊙ orcid.org/0000-0002-2633-9809; Email: jinhe@fiu.edu

Authors

Jing Guo – Department of Physics, Florida International University, Miami, Florida 33199, United States

Xingxu Yan — Department of Materials Science and Engineering and Irvine Materials Research Institute (IMRI), University of California, Irvine, California 92697, United States; orcid.org/0000-0001-7991-4849

Mingjie Xu — Irvine Materials Research Institute (IMRI), University of California, Irvine, California 92697, United States

Govinda Ghimire — Department of Physics, Florida International University, Miami, Florida 33199, United States

Xiaoqing Pan — Department of Materials Science and Engineering, Irvine Materials Research Institute (IMRI), and Department of Physics and Astronomy, University of California, Irvine, California 92697, United States;
orcid.org/0000-0002-0965-8568

Complete contact information is available at: https://pubs.acs.org/10.1021/acs.analchem.0c04398

Notes

The authors declare no competing financial interest.

ACKNOWLEDGMENTS

This work was supported by the Engineering Research Centers Program of the National Science Foundation (NSF) under NSF Cooperative Agreement no. EEC-1647837 and NSF (CBET1454544). The TEM work was supported by the NSF under the grant number CBET2031494. J.G. acknowledges the Dissertation Year Fellowship of the University Graduate School at Florida International University.

REFERENCES

- (1) Langer, J.; Jimenez de Aberasturi, D.; Aizpurua, J.; Alvarez-Puebla, R. A.; Auguié, B.; Baumberg, J. J.; Bazan, G. C.; Bell, S. E. J.; Boisen, A.; Brolo, A. G.; Choo, J.; Cialla-May, D.; Deckert, V.; Fabris, L.; Faulds, K.; García de Abajo, F. J.; Goodacre, R.; Graham, D.; Haes, A. J.; Haynes, C. L.; Huck, C.; Itoh, T.; Käll, M.; Kneipp, J.; Kotov, N. A.; Kuang, H.; Le Ru, E. C.; Lee, H. K.; Li, J.-F.; Ling, X. Y.; Maier, S. A.; Mayerhöfer, T.; Moskovits, M.; Murakoshi, K.; Nam, J.-M.; Nie, S.; Ozaki, Y.; Pastoriza-Santos, I.; Perez-Juste, J.; Popp, J.; Pucci, A.; Reich, S.; Ren, B.; Schatz, G. C.; Shegai, T.; Schlücker, S.; Tay, L.-L.; Thomas, K. G.; Tian, Z.-Q.; Van Duyne, R. P.; Vo-Dinh, T.; Wang, Y.; Willets, K. A.; Xu, C.; Xu, H.; Xu, Y.; Yamamoto, Y. S.; Zhao, B.; Liz-Marzán, L. M. ACS Nano 2020, 14, 28–117.
- (2) Martín Sabanés, N.; Ohto, T.; Andrienko, D.; Nagata, Y.; Domke, K. F. *Angew. Chem., Int. Ed.* **2017**, *56*, 9796–9801.
- (3) Holze, R. Phys. Chem. Chem. Phys. 2015, 17, 21364-21372.
- (4) Ma, C.; Harris, J. M. Langmuir 2011, 27, 3527-3533.
- (5) Cui, L.; Liu, B.; Vonlanthen, D.; Mayor, M.; Fu, Y.; Li, J.-F.; Wandlowski, T. J. Am. Chem. Soc. 2011, 133, 7332–7335.
- (6) Wu, D.-Y.; Li, J.-F.; Ren, B.; Tian, Z.-Q. Chem. Soc. Rev. 2008, 37, 1025-1041.
- (7) Rosendahl, S. M.; Burgess, I. J. Electrochim. Acta 2008, 53, 6759-6767.
- (8) Touzalin, T.; Joiret, S.; Maisonhaute, E.; Lucas, I. T. Anal. Chem. **2017**, 89, 8974–8980.
- (9) Lynk, T. P.; Sit, C. S.; Brosseau, C. L. Anal. Chem. 2018, 90, 12639-12646.
- (10) Bindesri, S. D.; Alhatab, D. S.; Brosseau, C. L. Analyst 2018, 143, 4128-4135.
- (11) Greene, B. H. C.; Alhatab, D. S.; Pye, C. C.; Brosseau, C. L. J. Phys. Chem. C 2017, 121, 8084–8090.
- (12) Zaleski, S.; Clark, K. A.; Smith, M. M.; Eilert, J. Y.; Doty, M.; Van Duyne, R. P. Anal. Chem. **2017**, 89, 2497–2504.
- (13) Smith, S. R.; Seenath, R.; Kulak, M. R.; Lipkowski, J. *Langmuir* **2015**, 31, 10076–10086.
- (14) Chen, Z.; Jiang, S.; Kang, G.; Nguyen, D.; Schatz, G. C.; Van Duyne, R. P. J. Am. Chem. Soc. 2019, 141, 15684–15692.
- (15) Zong, C.; Chen, C.-J.; Zhang, M.; Wu, D.-Y.; Ren, B. J. Am. Chem. Soc. 2015, 137, 11768–11774.
- (16) Kurouski, D.; Mattei, M.; Van Duyne, R. P. *Nano Lett.* **2015**, 15, 7956–7962.
- (17) Di Martino, G.; Turek, V. A.; Lombardi, A.; Szabó, I.; de Nijs, B.; Kuhn, A.; Rosta, E.; Baumberg, J. J. Nanosci. Lett. 2017, 17,
- (18) Di Martino, G.; Turek, V. A.; Tserkezis, C.; Lombardi, A.; Kuhn, A.; Baumberg, J. J. Faraday Discuss 2017, 205, 537–545.
- (19) Chen, Y. X.; Tian, Z. Q. Chem. Phys. Lett. 1997, 281, 379-383.
- (20) Lombardi, J. R.; Birke, R. L. J. Phys. Chem. C 2008, 112, 5605-5617.
- (21) Byers, C. P.; Zhang, H.; Swearer, D. F.; Yorulmaz, M.; Hoener, B. S.; Huang, D.; Hoggard, A.; Chang, W.-S.; Mulvaney, P.; Ringe, E.; Halas, N. J.; Nordlander, P.; Link, S.; Landes, C. F. Sci. Adv. 2015, 1, No. e1500988.
- (22) Chirea, M.; Collins, S. S. E.; Wei, X.; Mulvaney, P. Chem. Phys. Lett. 2014, 5, 4331–4335.
- (23) Liu, B.; Han, G.; Zhang, Z.; Liu, R.; Jiang, C.; Wang, S.; Han, M.-Y. Anal. Chem. **2012**, *84*, 255–261.
- (24) Hossain, M. K.; Kitahama, Y.; Huang, G. G.; Han, X.; Ozaki, Y. Anal. Bioanal. Chem. **2009**, 394, 1747–1760.
- (25) Huang, Y.; Ma, L.; Li, J.; Zhang, Z. Nanotechnology 2017, 28, 105203
- (26) Hoener, B. S.; Kirchner, S. R.; Heiderscheit, T. S.; Collins, S. S. E.; Chang, W.-S.; Link, S.; Landes, C. F. Chem **2018**, 4, 1560–1585.
- (27) Guo, J.; Pan, J.; Chang, S.; Wang, X.; Kong, N.; Yang, W.; He, J. Small **2018**, 14, 1704164.
- (28) Ai, Q.; Zhou, J.; Guo, J.; Pandey, P.; Liu, S.; Fu, Q.; Liu, Y.; Deng, C.; Chang, S.; Liang, F.; He, J. *Nanoscale* **2020**, *12*, 17103–17112.

- (29) Ma, T.; Guo, J.; Chang, S.; Wang, X.; Zhou, J.; Liang, F.; He, J. *Phys. Chem. Chem. Phys.* **2019**, *21*, 15940–15948.
- (30) Tuchband, M.; He, J.; Huang, S.; Lindsay, S. Rev. Sci. Instrum. 2012, 83, 015102.
- (31) Johnson, P. B.; Christy, R. W. Phys. Rev. B: Solid State 1972, 6, 4370-4379.
- (32) White, J. J.; Straley, J. W. J. Opt. Soc. Am. 1968, 58, 759-763.
- (33) Tilton, L. W.; Plyler, E. K.; Stephens, R. E. J. Opt. Soc. Am. 1950, 40, 540-543.
- (34) Zhao, J.; Bradbury, C. R.; Huclova, S.; Potapova, I.; Carrara, M.; Fermín, D. J. *J. Phys. Chem. B* **2005**, *109*, 22985–22994.
- (35) Starowicz, Z.; Wojnarowska-Nowak, R.; Ozga, P.; Sheregii, E. M. Colloid Polym. Sci. 2018, 296, 1029–1037.
- (36) Hill, C. M.; Bennett, R.; Zhou, C.; Street, S.; Zheng, J.; Pan, S. J. Phys. Chem. C **2015**, 119, 6760–6768.
- (37) Choi, Y.-J.; Luo, T.-J. M. Int. J. Electrochem. Sci. 2011, 2011, 1–
- (38) Oje, A. I.; Ogwu, A. A.; Mirzaeian, M.; Tsendzughul, N. J. Electroanal. Chem. **2018**, 829, 59–68.
- (39) Benz, F.; Tserkezis, C.; Herrmann, L. O.; de Nijs, B.; Sanders, A.; Sigle, D. O.; Pukenas, L.; Evans, S. D.; Aizpurua, J.; Baumberg, J. J. Nano Lett. 2015, 15, 669–674.
- (40) Benz, F.; Chikkaraddy, R.; Salmon, A.; Ohadi, H.; de Nijs, B.; Mertens, J.; Carnegie, C.; Bowman, R. W.; Baumberg, J. J. J. Phys. Chem. Lett. 2016, 7, 2264–2269.
- (41) Han, B.; Ma, N.; Yu, J.; Xiao, L.; Guo, S.; Park, E.; Jin, S.; Chen, L.; Jung, Y. M. Spectrochim. Acta, Part A 2020, 239, 118451.
- (42) Guo, L.; Zhang, X.; Li, P.; Han, R.; Liu, Y.; Han, X.; Zhao, B. New J. Chem. **2019**, 43, 230–237.
- (43) Xue, X.; Ruan, W.; Yang, L.; Ji, W.; Xie, Y.; Chen, L.; Song, W.; Zhao, B.; Lombardi, J. R. *J. Raman Spectrosc.* **2012**, *43*, 61–64.
- (44) Zhang, X.-Y.; Han, D.; Pang, Z.; Sun, Y.; Wang, Y.; Zhang, Y.; Yang, J.; Chen, L. J. Phys. Chem. C 2018, 122, 5599-5605.
- (45) Jiang, X.; Yin, D.; Yang, M.; Du, J.; Wang, W.; Zhang, L.; Yang, L.; Han, X.; Zhao, B. Appl. Surf. Sci. 2019, 487, 938–944.
- (46) Zhang, X.; Yu, Z.; Ji, W.; Sui, H.; Cong, Q.; Wang, X.; Zhao, B. J. Phys. Chem. C 2015, 119, 22439–22444.
- (47) Jiang, L.; You, T.; Yin, P.; Shang, Y.; Zhang, D.; Guo, L.; Yang, S. *Nanoscale* **2013**, *5*, 2784–2789.
- (48) Zhou, L.; Zhou, J.; Lai, W.; Yang, X.; Meng, J.; Su, L.; Gu, C.; Jiang, T.; Pun, E. Y. B.; Shao, L.; Petti, L.; Sun, X. W.; Jia, Z.; Li, Q.; Han, J. *Nat. Commun.* **2020**, *11*, 1785.